Chinese Journal of Mechanical Engineering

ORIGINAL ARTICLE

Open Access

Design and Analysis of a Novel Shoulder Exoskeleton Based on a Parallel Mechanism

Lianzheng Niu[1], Sheng Guo[1,2*], Majun Song[3], Yifan Wu[1] and Haibo Qu[1]

Abstract

Power-assisted upper-limb exoskeletons are primarily used to improve the handling efficiency and load capacity. However, kinematic mismatch between the kinematics and biological joints is a major problem in most existing exoskeletons, because it reduces the boosting effect and causes pain and long-term joint damage in humans. In this study, a shoulder augmentation exoskeleton was designed based on a parallel mechanism that solves the shoulder dislocation problem using the upper arm as a passive limb. Consequently, the human–machine synergy and wearability of the exoskeleton system were improved without increasing the volume and weight of the system. A parallel mechanism was used as the structural body of the shoulder joint exoskeleton, and its workspace, dexterity, and stiffness were analyzed. Additionally, an ergonomic model was developed using the principle of virtual work, and a case analysis was performed considering the lifting of heavy objects. The results show that the upper arm reduces the driving force requirement in coordinated motion, enhances the load capacity of the system, and achieves excellent assistance.

Keywords Upper limb exoskeleton, Parallel mechanism, Human–machine compatibility, Dynamics

1 Introduction

Exoskeleton robots are a special class of human–robot collaborative robots worn during an operation to realize the seamless combination of the powerful driving ability of the robot and the developed intelligence of the human body [1]. Therefore, the study of power-assisted upper-limb exoskeleton devices is essential in exoskeleton robotics, which is mainly aimed at normal people with healthy bodies. Using a reasonable mechanical structure design, the upper limbs of the operator can be used to carry, push, pull, lift, and perform other actions to improve the handling efficiency and load capacity. Simultaneously, this reduces the persistent problems of invisible occupational diseases in the labor force.

Currently, several scholars have designed various types of upper-limb exoskeleton robots. One type is an exoskeleton device with a rigid structure that is isomorphic to the upper limbs of the human body [2–5]. As this type of design is based on mapping the degrees of freedom of the human biological joints onto an exoskeleton device and then projecting the joint moments onto the corresponding degrees of freedom of the human joints via external actuation, it relies heavily on the synergy of human–machine movements. Furthermore, this type of exoskeleton suffers from low accuracy of the end-effector control inherent in a tandem structure [6]. Practically, it is difficult to accurately replicate all joint degrees of freedom and ensure that they align with the human degrees of freedom [7]. Here, the shoulder complex was considered as one of the most representative examples. In addition to the three rotational degrees of freedom of the glenohumeral joint, the sternoclavicular joint provides

*Correspondence:
Sheng Guo
shguo@bjtu.edu.cn
[1] School of Mechanical, Electronic and Control Engineering, Beijing Jiaotong University, Beijing 100044, China
[2] Key Laboratory of Vehicle Advanced Manufacturing, Measuring and Control Technology, Ministry of Education, Beijing Jiaotong University, Beijing 100044, China
[3] Hangzhou Innovation Institute, Beihang University, Hangzhou 100044, China

the shoulder joint with two additional translational degrees of freedom. Moreover, these additional degrees of freedom are not entirely independent; they evolve with the arm's abduction/adduction and flexion/extension motions. Consequently, when the degrees of freedom of the robot and the joints of the human body are not accurately aligned, the robot generates parasitic forces at the attachment points and reacts to the joints themselves, leading to a range of human–computer interaction problems during practical use. This reduces the boosting effect and causes pain and prolonged joint damage [8, 9].

In most existing exoskeletons, mechanical and biological joint misalignments result in excessive human–computer interactions, causing injury to the wearer. To solve the problem of joint mismatch, the wearable comfort needs to be improved. Some scholars have proposed manual alignment to solve joint dislocation [10, 11]; however, manual alignment is typically inaccurate and the effectiveness of this strategy is quite limited because all the different factors causing dislocation cannot be explained, and their performance with respect to the other factors is highly dependent on the precision of wearing. The use of compatible elements is also an effective method of solving the joint dislocation problem. For example, the joint axis can be replaced by a compliant mechanism that derives its disorientation from elastic deformation. The disadvantage of using these elements is that owing to their nature, the motion of the joint is always accompanied by torque around the axis of the joint. If a zero-torque operation is required, an additional actuator must be introduced to counteract the passive torque generated by joint flexion [12]. Some scholars have also attempted to realize the adaptive compensation of the exoskeleton and corresponding joints in the human body during auxiliary motion by increasing the redundant degrees of freedom or equipping auxiliary mechanisms, which is also a mainstream method of solving joint mismatch problem [13]. For example, Ergin et al. [14] proposed adjusting the joint center of the upper-limb exoskeleton robot by increasing the corresponding active degrees of freedom to achieve decent human–computer interaction. Yan et al. [15] proposed a 3-degree-of-freedom (DOF) shoulder exoskeleton that can adjust the joint center by increasing the passive degree of freedom, which significantly facilitates anthropomorphic design. Dehez et al. [16] proposed a different type of robot specially used for shoulder training, whose adaptive structure and action principle enabled the robot to maximize the ergonomic effects during installation and training. However, the above design complicated the overall structure of the exoskeleton, which significantly increased the structure's volume and weight. This caused it fall short of the design requirements of a portable and wearable exoskeletons, and limited the auxiliary effect of the exoskeleton robot. To solve the problem of incompatibility between the upper-limb exoskeleton and human movement and to reduce the system mass as much as possible, the fully-flexible exoskeleton was proposed and has become a research hotspot. Compared with a rigid upper-limb exoskeleton, a flexible exoskeleton eliminates the rigid structure, physically eliminates the problem of joint dislocation, and provides a higher wearing comfort [17–20]. However, some common disadvantages of fully-flexible exoskeletons are that useful boosting effects cannot be achieved without a rigid substrate and flexible exoskeletons require expensive manufacturing materials. Parallel mechanisms can achieve better inertial characteristics while maintaining lightweight and compactness. An adaptive mechanism with only passive joints was introduced to compensate for exoskeleton-limb dislocation and the size changes between the different subjects, which is an effective method of solving the joint mismatch problem [21]. Recently, researchers have adopted different structures to solve human joint dislocation problems such as that in a parallel hip exoskeleton based on the 3-UPS/S configuration proposed by Zhang et al. [22]. YU et al. [23] proposed the same structure and conducted a series of kinematic analyses. Klein et al. proposed an upper-limb exoskeleton with a parallel mechanism to drive the motion of the shoulder joint and realize its rotation through the space-staggered motion of two rods [24]. The parallel shoulder exoskeleton developed by Hunter et al. assists the shoulder joint by binding to the human arm to actuate arm movement, thereby accommodating the shift in the center of rotation of the human shoulder joint during actual movement [25]. However, owing to the large number of limbs and actuators in the aforementioned parallel mechanism, wearability has become the biggest problem in the practical application of parallel exoskeletons. Therefore, a feasible approach for improving human–machine compatibility is to design a parallel exoskeleton with adaptive biological joint rotation center characteristics and fewer limb distributions. Therefore, a human upper arm with a self-adaptive rotation center is proposed in this study as the passive limb based on the parallel mechanism, and two fewer driving limbs are used to form the parallel shoulder exoskeleton to solve the shoulder mismatch problem at the human–machine compatibility level.

In this study, we designed a wearable upper-limb exoskeleton robot based on the 2-UPR-SR parallel mechanism. The upper arm, shoulder joint, and elbow joint of the human body were used as the passive limb SR of the parallel mechanism, and the two UPR limbs were used as the driving limbs to realize motion assistance with two degrees of freedom of flexion/extension and adduction/

abduction of the human upper limb, where P denotes the drive pair, R (revolute), P (prismatic), U (universal), C (cylinder), and S (spherical). The human–machine compatible parallel exoskeleton designed in this study not only helps to solve the problem of shoulder dislocation and improves the wearing comfort, but also increases the stiffness and stability of the exoskeleton system using the characteristics of the parallel mechanism, giving it a higher load-bearing capacity and excellent power-assist potential. Additionally, the use of fewer drive motors can reduce control defects [26], thereby promoting the practical application of exoskeletons.

The remainder of this study is organized as follows: Section 2 presents the motion mechanism of the upper limbs of the human body, the design of the 2-UPR-SR parallel upper-limb exoskeleton mechanism based on the motion requirements, and complete the verification of the freedom. Section 3 presents the kinematic performance of the 2-UPR-SR parallel upper-limb exoskeleton including the inverse kinematics, workspace, dexterity, and stiffness. Human–machine dynamics modeling is described in Section 4, with theoretical validation and case studies presented in Section 5. Finally, conclusions are drawn in Section 6.

2 Conceptual Design and Mobile Verification

2.1 Upper Limb Movement Mechanism

Shoulder-joint movements are usually divided into shoulder joint adduction/abduction, shoulder joint flexion/extension, and shoulder joint internal/external rotation, as shown in Figure 1. However, because the kinematic manifestations of the external and internal rotations of the shoulder were not active, they were not considered in this study.

The focus of this study is to achieve good human–machine compatibility and solve the shoulder joint mismatch problem while also considering the simplicity and practicality of the exoskeleton mechanism. Based on this, a parallel 2-UPR-SR mechanism with a passive limb that can satisfy two degrees of freedom for human flexion/

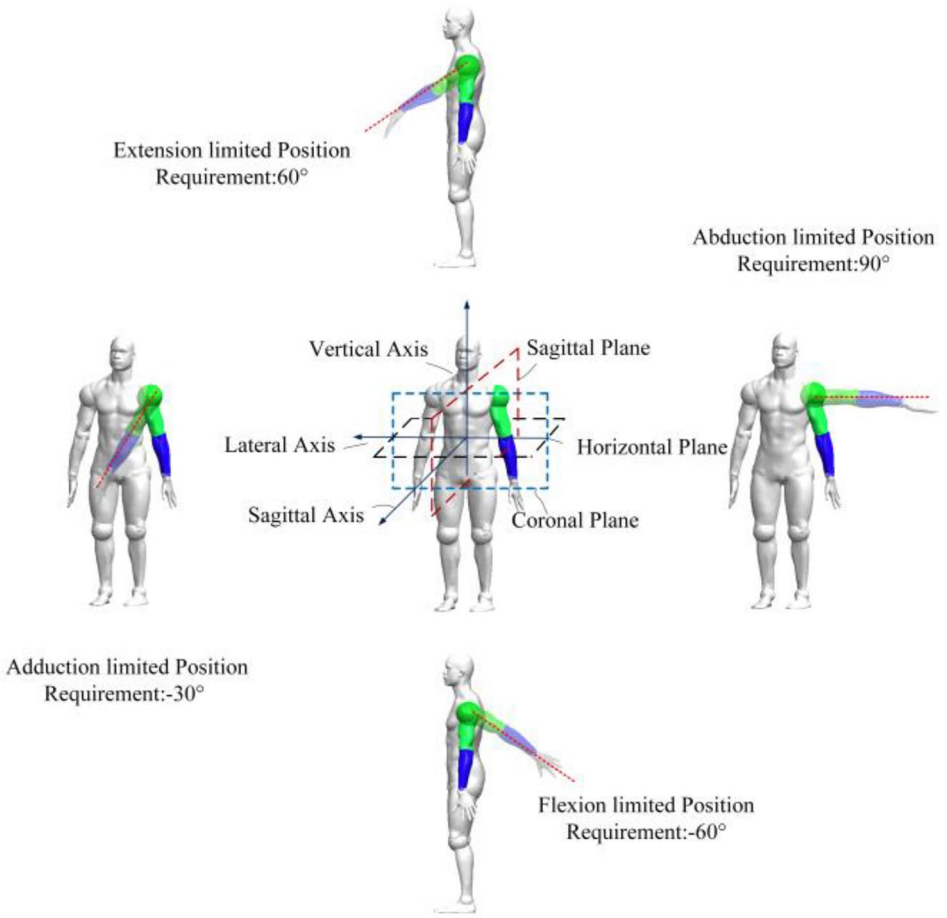

Figure 1 Motion characteristics of the human upper arm

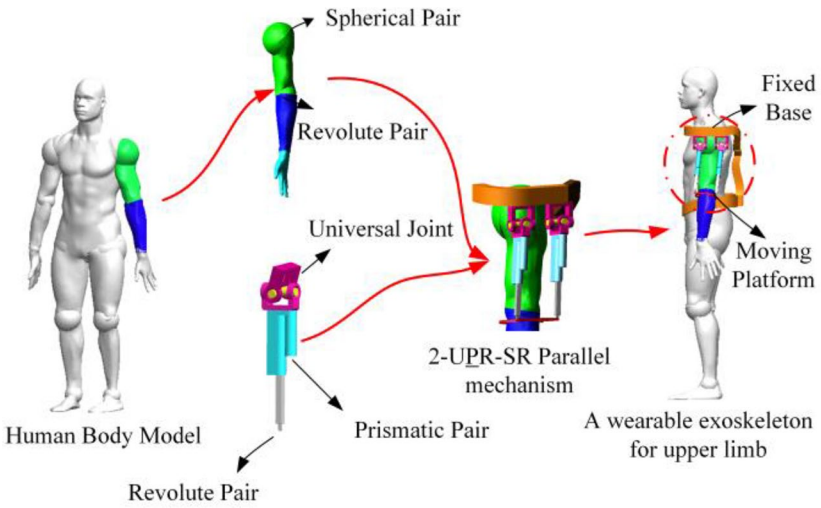

Figure 2 Upper limb exoskeleton design process

extension and internal retraction/abduction movements was designed. The neglected internal/external rotation degrees of freedom were used less than the other two degrees of freedom, which is similar to the simplifications made in literature [27, 28]. It is worth noting that the movement of the shoulder joint involves both the movement of the shoulder joint itself and the movement of the shoulder girdle (clavicle and scapula), which is called the scapulohumeral rhythm [29]. For example, for every 15° of upper arm elevation, the glenohumeral joint was rotated by 10° and the scapula by 5°. The range of motion was approximately 2:1 (possibly 1.25:1 or 1.35:1). Consequently, during shoulder joint motion in the vertical plane, the instantaneous center of joint rotation increases with the arm elevation, which causes joint dislocations and makes the design of upper-limb exoskeletons more difficult.

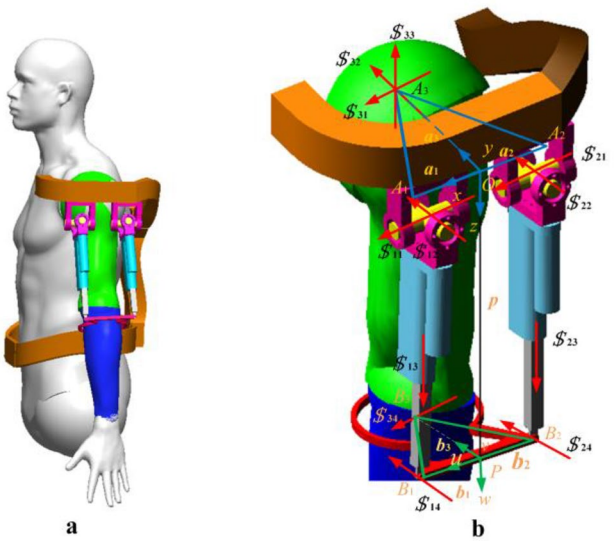

Figure 3 Upper-limb exoskeleton: **a** Wearing effect and **b** 2-UPR-SR parallel mechanism

2.2 Configuration Design

Whether the exoskeleton robot is serial or parallel, it comprises the most basic elements such as rods and kinematics. The joints can be divided into R (revolute), P (prismatic), U (universal), C (cylindrical), and S (spherical) joints. To design an upper-limb shoulder exoskeleton that meets these requirements, the following five design criteria must be satisfied:

(1) The shoulder joint of the upper arm of the human body should be regarded as a ball pair and the elbow joint as a rotating pair that is part of the limb of the upper limb of the human body.
(2) To ensure the stability of the upper-limb exoskeleton, the proposed mechanism configuration must be symmetrical according to the anatomical characteristics of the upper limbs. The two drive limbs in this mechanism should have the same configuration and be symmetrical about the upper limb.
(3) The mechanism should have a large-angle rotation function to realize the flexion and extension of the shoulder joint and adduction/abduction movements. Each limb should have at least one rotating pair connected to a fixed platform, and the axis of the rotating pair should be parallel to the horizontal axis of the human body. To achieve the flexion-extension kinematic characteristics of the elbow

joint, each strut limb should have at least one rotational sub-connection to the mobile platform, the axis of which is parallel to the sagittal axis of the body.

(4) To ensure the stability of the mechanism and offset the displacement caused by the change in the shoulder joint center, each drive limb should have at least one moving pair and should not be installed on the fixed and moving platforms.

(5) Each limb (except the upper arm) of the parallel mechanism should be uniformly arranged into three joints to obtain excellent stability and better motion characteristics.

Generally, there are two methods for proposing a modern parallel mechanism. The first is a direct-type composition using the screw theory, Lie group theory, GF group theory, or any other method. The second approach involves adding passive limbs to an existing parallel mechanism to constrain the undesired degrees of freedom [30–32]. However, the passive limbs add weight and complexity to the mechanism. Therefore, passive limbs with simple structures should be selected as frequently as possible, provided that the requirements for use are met. According to research on the mechanism of the human anatomy, the shoulder joint of the upper limb of the human body is equivalent to the S joint, and the elbow joint is equivalent to the R joint [33]. A comprehensive passive limb was not chosen in this study. However, the human shoulder and elbow joints were integrated into the 2-UPR parallel mechanism as passive SR limbs according to the design criteria to realize 2 degrees of freedom of flexion and extension, and the adduction and abduction collaborative movement of the human upper limb. After being worn on the human body, the shoulder platform became fixed platform, and the connecting ring at the forearm became a mobile platform. In this parallel mechanism, the drive limb from the base to the platform consists of a universal joint, a prismatic joint, and a rotary joint connected to the moving platform, and the driving pair P consists of a sleeve and a piston rod in the middle, as shown in Figure 2. It is important to note that the platform described here is not fixed in the conventional sense. Because the upper arm is connected to the fixed platform as the passive limb of the parallel mechanism, the fixed platform rises with the lifting of the arm limb, and adaptive compensation for the motion in vertical plane of shoulder joint is required.

2.3 Degree of Freedom Verification

A fixed bracket equivalent to the fixed platform of the parallel mechanism is designed on the shoulder. The position where the upper arm muscles exert force is equivalent to the moving platform of the parallel mechanism, which drives the upper arm to move relative to the fixed platform. Among them, the fixed platform $\Delta A_1A_2A_3$ and the moving platform $\Delta B_1B_2B_3$ are both equilateral triangles with side lengths $2a$ and $2b$, respectively. *O-xyz* is the fiducial coordinate of the parallel mechanism and the origin O_0 is located at the center of the side length A_1A_2. The *P-uvw* is a moving frame with the origin P_0 at the midpoint of the side length B_1B_2. In this study, a right-handed coordinate system was used to construct a schematic of the 2-UPR-SR parallelism mechanism, as shown in Figure 3.

The kinematic properties of the 2-UPR-SR parallel mechanism were verified using the screw theory. The three limbs of the helix of motion of the 2-UPR-SR parallel mechanism are as follows:

$$\begin{cases} \$_{11} = \$_{21} = [\,1\ 0\ 0;\ \ 0\ 0\ 0\,]^{\mathrm{T}}, \\ \$_{12} = \$_{22} = [\,0\ 1\ 0;\ 0\ 0\ 1\,]^{\mathrm{T}}, \\ \$_{13} = \$_{23} = [\,0\ 0\ 0;\ l_1\ 0\ n_1\,]^{\mathrm{T}}, \\ \$_{14} = \$_{24} = [\,0\ 1\ 0;\ l_2\ 0\ n_2\,]^{\mathrm{T}}, \end{cases} \tag{1}$$

$$\begin{cases} \$_{31} = [\,1\ 0\ 0;\ 0\ 0\ -1\,]^{\mathrm{T}}, \\ \$_{32} = [\,0\ 1\ 0;\ 0\ 0\ 0\,]^{\mathrm{T}}, \\ \$_{33} = [\,0\ 0\ 1;\ -1\ 0\ 0\,]^{\mathrm{T}}, \\ \$_{34} = [\,1\ 0\ 0;\ 0\ m_1\ n_3\,]^{\mathrm{T}}. \end{cases} \tag{2}$$

Using the reciprocal product principle, the mechanism for constraining the screw is

$$\begin{cases} \$_1^r = [\,0\ 1\ 0\ 0\ 0\ 0\,]^{\mathrm{T}}, \\ \$_2^r = [\,0\ 0\ 0\ 0\ 0\ 1\,]^{\mathrm{T}}, \\ \$_3^r = [\,0\ -(1+n_3/m_1)\ 1;\ 1\ 0\ 0\,]^{\mathrm{T}}, \\ \$_4^r = [\,1\ 0\ 0;\ 0\ 0\ 1\,]^{\mathrm{T}}. \end{cases} \tag{3}$$

Additionally, the movement screw of the mechanism is

$$\begin{cases} \$_1 = [\,0\ 1\ 0;\ 0\ 0\ 0\,]^{\mathrm{T}}, \\ \$_2 = [\,1\ 0\ 0;\ 0\ 0\ -1\,]^{\mathrm{T}}. \end{cases} \tag{4}$$

The motion screw $\$$ is composed of two motion subhelixes $\$_1$ and $\$_2$. The validation results show that the 2-UPR-SR parallel mechanism has two pure rotational degrees of freedom around the x and y axes and can follow the upper arm of the human body for complete flexion/extension and adduction/abduction motion.

3 Kinematic Performance Verification of the 2-UPR-SR Parallel Mechanism

3.1 Kinematic Analysis

The inverse kinematics solution is based on the screw pose of the moving platform, and the drive joint variable values of each active limb are typically reversed [34]. Assuming that the initial position of the moving platform is identical to that of the fixed platform when the moving platform completes any rotation in space, the final pose can be represented using the rotation matrix $\boldsymbol{R}_B^A$ about the Euler angles. Assuming that the final posture of the moving platform is obtained by rotating α around the x-axis and β around the y-axis, the transformation matrix obtained using the Euler angle expression is

$$\boldsymbol{R}_B^A = \begin{bmatrix} a\cos\beta & \sin\beta\sin\alpha & \sin\beta\cos\alpha \\ 0 & \cos\alpha & -\sin\alpha \\ -\sin\beta & \cos\beta\sin\alpha & \cos\beta\cos\alpha \end{bmatrix}. \tag{5}$$

The position vector expression for each vertex on the fixed platform in the fixed platform coordinate system was obtained as follows:

$$\begin{cases} \boldsymbol{a}_1^o = [a \quad 0 \quad 0]^{\mathrm{T}}, \\ \boldsymbol{a}_2^o = [-a \quad 0 \quad 0]^{\mathrm{T}}, \\ \boldsymbol{a}_3^o = [0 \quad \sqrt{3}a \quad 0]^{\mathrm{T}}. \end{cases} \tag{6}$$

Moreover, the position vector expression of each vertex on the moving platform in the moving platform coordinate system is

$$\begin{cases} \boldsymbol{b}_1^p = [\,b \;\; 0 \;\; 0\,]^{\mathrm{T}}, \\ \boldsymbol{b}_2^p = [\,-b \;\; 0 \;\; 0\,]^{\mathrm{T}}, \\ \boldsymbol{b}_3^p = [\,0 \;\; \sqrt{3}b \;\; 0\,]^{\mathrm{T}}. \end{cases} \tag{7}$$

The superscript in Eq. (7) indicates that it is expressed in a coordinate system. Supposing that the original $\boldsymbol{p}$ of the moving coordinate system is the position vector $\boldsymbol{p}^o$ of the fixed coordinate system, the position vector expression for each vertex $\boldsymbol{B}_i$ on the moving platform in the coordinate system of the fixed platform is

$$\boldsymbol{b}_i^o = \boldsymbol{R}_B^A \boldsymbol{b}_i^p + \boldsymbol{p}^o \ . \tag{8}$$

Further, based on the vector relationship,

$$l_i \boldsymbol{s}_i = \boldsymbol{b}_i^o - \boldsymbol{a}_i^o, \tag{9}$$

where $\boldsymbol{s}_i$ is the unit vector pointing from A_i to B_i, l_i is the length of the i-th limb, and i=1, 2, and 3. To obtain the length of each limb, the $\boldsymbol{s}_i$ term is eliminated and both sides of the above equation are squared.

$$l_1 = \sqrt{\left(x_p + b\cos\beta - a\right)^2 + y_p^2 + \left(z_p - b\sin\beta\right)^2}, \tag{10}$$

$$l_2 = \sqrt{\left(x_p - b\cos\beta + a\right)^2 + y_p^2 + \left(z_p + b\sin\beta\right)^2}. \tag{11}$$

The position vector of each vertex $\boldsymbol{B}_i$ on the moving platform in the fixed platform coordinate system can also be expressed as

$$\boldsymbol{b}_3^o = \left[\, l_3\sin\beta\cos\alpha \;\; l_3\sin\alpha + \sqrt{3}a \;\; l_3\cos\beta\cos\alpha \,\right]^{\mathrm{T}}. \tag{12}$$

Simultaneously, Eqs. (9) and (12) were used to obtain the position vector of the center $\boldsymbol{p}$ of the moving platform.

$$\boldsymbol{p} = \begin{bmatrix} x_p \\ y_p \\ z_p \end{bmatrix} = \begin{bmatrix} l_3\sin\beta\cos\alpha - \sqrt{3}b\sin\beta\sin\alpha \\ -l_3\sin\alpha + \sqrt{3}a - \sqrt{3}b\cos\alpha \\ l_3\cos\beta\cos\alpha - \sqrt{3}b\cos\beta\sin\alpha \end{bmatrix}. \tag{13}$$

3.2 Fully Jacobian Matrix

The Jacobian matrix reflects the speed mapping relationship between the drive input of the linkage mechanism and output of the moving platform, and is one of the critical indicators for the performance evaluation of the parallel mechanism [35]. In this study, the relationship between the motions and constraints of the 2-UPR-SR parallel mechanism limbs were used to construct a Jacobian matrix of the motions and constraints of each limb using the screw theory, which was then employed in establishing the full Jacobian matrix of the mechanism.

Here, the instantaneous motion screw of the parallel mechanism moving platform is expressed as $\$_p = [\,\boldsymbol{w}_p \;\; \boldsymbol{v}_p\,]^{\mathrm{T}}$, where $\boldsymbol{W}_p$ is the angular velocity vector of the moving platform, and $\boldsymbol{V}_p$ is the linear velocity vector when any point of the moving platform is instantaneously coincident with the origin of the base coordinate system. For the instantaneous motion characteristics of the moving platform, the joint restraint of the moving platform from the ends of each limb was solved using a linear combination based on the motion of each limb and constraint screw.

$\$_{j,i}$ was used to represent the unit screw of the j-th (j = 1,2,3,4) kinematic pair in the i-th (i = 1,2) UPR limb.

The UPR limb had three passive pairs and one active pair. To facilitate characterization, the multi-DOF joints must be equivalent to the combined form of single-DOF joints. Therefore, each limb can be regarded as an open-loop kinematic chain composed of several single-degree-of-freedom kinematic pairs, the ends of which are connected to the motion platform. For convenience of analysis, the origin defining the instantaneous reference frame {*Bs*} is located at point *P*, and the x_s, y_s, and z_s axes are parallel to the x, y, and z axes in the reference frame {A}, respectively.

The instantaneous speed $\$_p$ generated by the UPR limb on the moving platform can be expressed as

$$\$_p = \dot{\theta}_{1,i}\hat{\$}_{1,i} + \dot{\theta}_{2,i}\hat{\$}_{2,i} + \dot{q}_i\hat{\$}_{3,i} + \dot{\theta}_{4,i}\hat{\$}_{4,i}, \tag{14}$$

where $\dot{\theta}_{j,i}$ is the rotational angular velocity of the j-th rotating pair in the i-th limb, and $\dot{q}_i$ is the linear velocity of the moving pair in the i-th limb. The UPR limb has three passive pairs and one active pair, which can be expressed for each screw in the instantaneous reference frame as

$$\begin{cases} \hat{\$}_{1,i} = \begin{bmatrix} \boldsymbol{s}_{1,i} \\ (\boldsymbol{b}_i - \boldsymbol{l}_i) \times \boldsymbol{s}_{1,i} \end{bmatrix}, \\ \hat{\$}_{2,i} = \begin{bmatrix} \boldsymbol{s}_{2,i} \\ (\boldsymbol{b}_i - \boldsymbol{l}_i) \times \boldsymbol{s}_{2,i} \end{bmatrix}, \\ \hat{\$}_{3,i} = \begin{bmatrix} 0 \\ \boldsymbol{s}_{3,i} \end{bmatrix}, \\ \hat{\$}_{4,i} = \begin{bmatrix} \boldsymbol{s}_{4,i} \\ \boldsymbol{b}_i \times \boldsymbol{s}_{4,i} \end{bmatrix}, \end{cases} \tag{15}$$

where $i = 1, 2$. Additionally, the antispin is obtained using the screw theory as follows:

$$\begin{cases} \hat{\$}^r_{1,i} = \begin{bmatrix} \boldsymbol{s}_{2,i} \\ (\boldsymbol{b}_i - \boldsymbol{l}_i) \times \boldsymbol{s}_{2,i} \end{bmatrix}, \\ \hat{\$}^r_{2,i} = \begin{bmatrix} 0 \\ \boldsymbol{s}_{3,i} \end{bmatrix}. \end{cases} \tag{16}$$

Table 1 Upper limb exoskeleton design parameters

Attributes	Value
Cylinder Length(mm)	180
Piston Length(mm)	180
Upper Arm l_3(mm)	320
Fixed platform side length a(mm)	60
Moving platform side length b(mm)	65
Cylinder Length(mm)	180
Piston Length(mm)	180

The point-multiplying constraint screws on both sides of Eq. (14) should satisfy the following equation:

$$\begin{cases} \hat{\$}^{r\mathrm{T}}_{1,i} \cdot \$_p = 0, \\ \hat{\$}^{r\mathrm{T}}_{2,i} \cdot \$_p = 0. \end{cases} \tag{17}$$

Therefore, the constrained Jacobian of the two limbed UPR is

$$\boldsymbol{J}_c = \begin{bmatrix} (\boldsymbol{b}_1 - \boldsymbol{l}_1) \times \boldsymbol{s}_{2,1})^{\mathrm{T}} & \boldsymbol{s}^{\mathrm{T}}_{2,1} \\ \boldsymbol{s}^{\mathrm{T}}_{3,1} & 0 \end{bmatrix}. \tag{18}$$

For the Jacobian analysis of the motion of the active limb, the moving pair in the UPR of the limb was locked, and the active limb was changed from a two-constrained screw system to a three-constrained screw

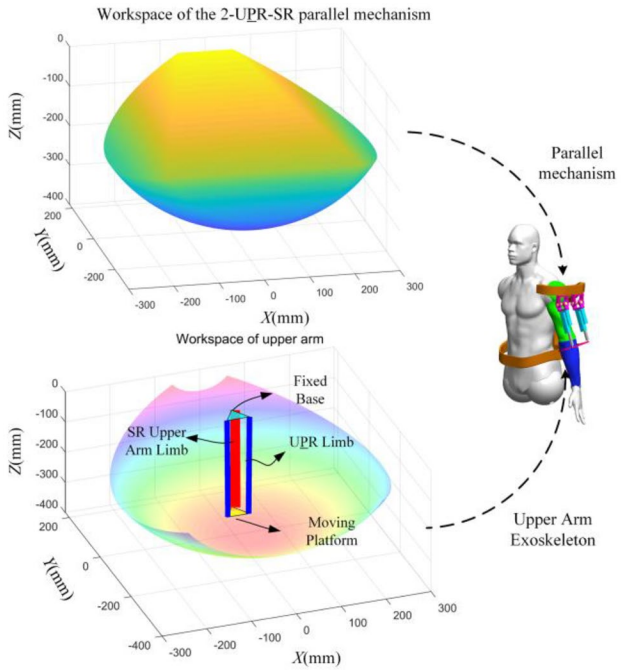

Figure 4 Shoulder exoskeleton workspace

system. Compared with Eq. (18), the addition of a constraining screw yields

$$\hat{\$}_{3,i}^{r} = \begin{bmatrix} \boldsymbol{s}_{3,i} \\ \boldsymbol{b}_i \times \boldsymbol{s}_{3,i} \end{bmatrix}. \tag{19}$$

By dot-multiplying the constraint screw in Eq. (14), we obtain

$$\hat{\$}_{3,i}^{r} \cdot \$_p = q_i. \tag{20}$$

The motion Jacobian matrix in the two-limbed UPR limbs is obtained as

$$\boldsymbol{J}_k = \begin{bmatrix} (\boldsymbol{b}_1 \times \boldsymbol{s}_{3,1})^{\mathrm{T}} & \boldsymbol{s}_{3,1}^{\mathrm{T}} \\ (\boldsymbol{b}_2 \times \boldsymbol{s}_{3,2})^{\mathrm{T}} & \boldsymbol{s}_{3,2}^{\mathrm{T}} \end{bmatrix}, \tag{21}$$

where $\$_{j,3}$ represents the screw of the j-th (j = 1,2,3,4) kinematic pair in the SR limb. The SR limb has four passive joint screws that can be expressed in the instantaneous reference frame as

$$\begin{cases} \hat{\$}_{1,3} = \begin{bmatrix} \boldsymbol{s}_{1,3} \\ (\boldsymbol{b}_3 - \boldsymbol{l}_3) \times \boldsymbol{s}_{1,3} \end{bmatrix}, \\ \hat{\$}_{2,3} = \begin{bmatrix} \boldsymbol{s}_{2,3} \\ (\boldsymbol{b}_3 - \boldsymbol{l}_3) \times \boldsymbol{s}_{2,3} \end{bmatrix}, \\ \hat{\$}_{3,3} = \begin{bmatrix} \boldsymbol{s}_{3,3} \\ (\boldsymbol{b}_3 - \boldsymbol{l}_3) \times \boldsymbol{s}_{3,3} \end{bmatrix}, \\ \hat{\$}_{4,3} = \begin{bmatrix} \boldsymbol{s}_{4,3} \\ \boldsymbol{b}_3^{Bs} \times \boldsymbol{s}_{4,3} \end{bmatrix}. \end{cases} \tag{22}$$

The instantaneous speed generated by the SR limb on the moving platform can be expressed as

$$\$_p = \dot{\theta}_{1,3}\hat{\$}_{1,3} + \dot{\theta}_{2,3}\hat{\$}_{2,3} + \dot{\theta}_{3,3}\hat{\$}_{3,3} + \dot{\theta}_{4,3}\hat{\$}_{4,3}. \tag{23}$$

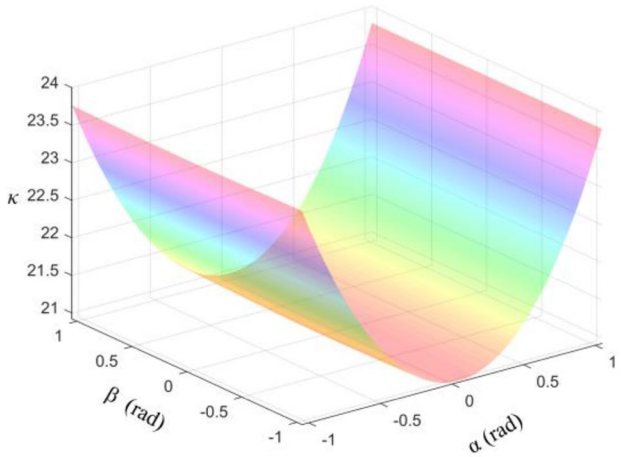

Figure 5 Dexterity graphs for Jacobian condition number

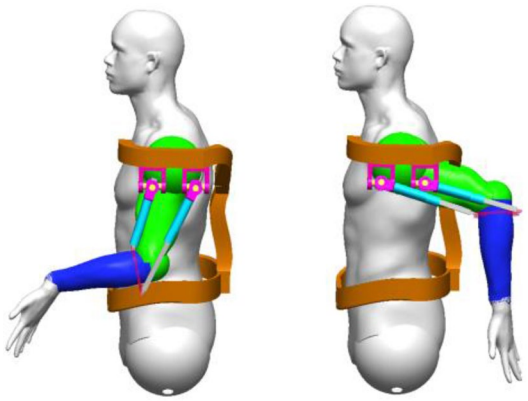

Figure 6 Elbow joint flexibility

The point product of both sides of Eq. (23) constrained screw satisfies the following:

$$\begin{cases} \hat{\$}_{1,3}^{r\mathrm{T}} \cdot \$_p = 0, \\ \hat{\$}_{2,3}^{r\mathrm{T}} \cdot \$_p = 0. \end{cases} \tag{24}$$

Therefore, the constraint Jacobian of the limb SR is

$$\boldsymbol{J}_c = \begin{bmatrix} ((\boldsymbol{b}_3 - \boldsymbol{l}_3) \times \boldsymbol{s}_{1,3})^{\mathrm{T}} & \boldsymbol{s}_{1,3}^{\mathrm{T}} \\ ((\boldsymbol{b}_3 - \boldsymbol{l}_3) \times \boldsymbol{s}_{3,3})^{\mathrm{T}} & \boldsymbol{s}_{3,3}^{\mathrm{T}} \end{bmatrix}. \tag{25}$$

Then, the complete Jacobian matrix of 2-UPR-SR is

$$\boldsymbol{J} = \begin{bmatrix} (\boldsymbol{b}_1 \times \boldsymbol{s}_{3,1})^{\mathrm{T}} & \boldsymbol{s}_{3,1}^{\mathrm{T}} \\ (\boldsymbol{b}_2 \times \boldsymbol{s}_{3,2})^{\mathrm{T}} & \boldsymbol{s}_{3,2}^{\mathrm{T}} \\ ((\boldsymbol{b}_1 - \boldsymbol{l}_1) \times \boldsymbol{s}_{2,1})^{\mathrm{T}} & \boldsymbol{s}_{2,1}^{\mathrm{T}} \\ \boldsymbol{s}_{3,1}^{\mathrm{T}} & 0 \\ ((\boldsymbol{b}_3 - \boldsymbol{l}_3) \times \boldsymbol{s}_{1,3})^{\mathrm{T}} & \boldsymbol{s}_{1,3}^{\mathrm{T}} \\ ((\boldsymbol{b}_3 - \boldsymbol{l}_3) \times \boldsymbol{s}_{3,3})^{\mathrm{T}} & \boldsymbol{s}_{3,3}^{\mathrm{T}} \end{bmatrix}. \tag{26}$$

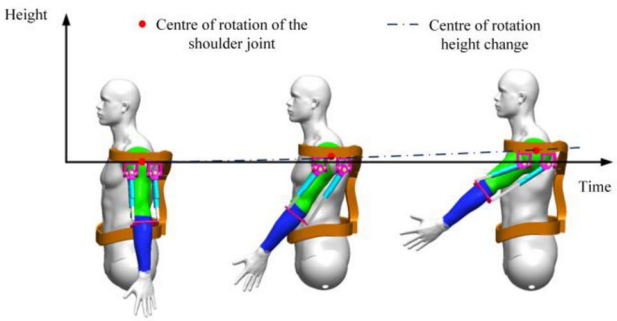

Figure 7 Adaptation of the shoulder joint to the shoulder-humeral rhythm

3.3 Kinematic Performance Verification

3.3.1 Workspace

The workspace of a parallel robot refers to the working area of the manipulator or bounded area where the manipulator operates on the moving platform. Their size is an essential metric for measuring the performance of parallel mechanisms. Workspaces are classified into reachable and flexible workspaces [36]. Workspace analysis was performed to ensure that the rotation of the 2-UPR-SR parallel mechanism around the *x*- and *y*-axes was consistent with the motion characteristics of the upper limb. The numerical method for solving the workspace is based on the inverse solution of the pose of a parallel robot. By determining the position of the end of the mechanism, the coordinate search method [37] can be used to obtain the working space of the mechanism under various constraints. In this regard, the three-dimensional spatial range of motion of the 2-UPR-SR parallel mechanism is shown in Figure 4.

The results of the study show that the mechanism has a good three-dimensional motion space, can meet task requirements, and has no singularity in its range of motion. The workspace around the *y*-axis satisfies the upper arm adduction/abduction range of motion (−30°–90°) and has symmetry around the *x*-axis, thereby meeting the upper arm extension/flexion range of motion (−60°–60°). The simulation parameters are listed in Table 1.

3.3.2 Dexterity and Stiffness Analysis

The singular configuration of the parallel mechanism is slightly more complicated. When the determinant of the Jacobian matrix of the robot is zero or tends toward infinity, the robot is stiffened or has redundant degrees of freedom, and the motion is uncertain. This is mainly because when the robot approaches a singular configuration, its Jacobian matrix is ill-distributed, distorting the transfer between the input and output of the motion [38, 39]. Therefore, dexterity is an index that quantitatively measures the degree of movement. A superior dexterity indicates that the mechanism has a high stability and movement efficiency. However, this type of mechanism design should be located as far away from singular configurations. Currently, the dexterity of a robot is measured using the Jacobian condition number.

The condition number of the Jacobian matrix can be defined as follows:

$$\kappa(\boldsymbol{J}) = \|\boldsymbol{J}\| \left\|\boldsymbol{J}^{-1}\right\|, \tag{27}$$

and

$$\|\boldsymbol{J}\| = \max_{\|x=1\|} \|\boldsymbol{J}x\|. \tag{28}$$

Taking the square of both sides of the equation, we obtain the following:

$$\|\boldsymbol{J}\|^2 = \max_{\|x=1\|} \boldsymbol{x}^{\mathrm{T}} \boldsymbol{J}^{\mathrm{T}} \boldsymbol{J} x, \tag{29}$$

where $\|\boldsymbol{J}\|^2$ is the largest eigenvalue in the matrix $\boldsymbol{J}^{\mathrm{T}}\boldsymbol{J}$; therefore, the $\boldsymbol{J}$ spectral norm is the largest singular value $\sigma_{\max}$ in the matrix, and can be obtained as:

$$\kappa(\boldsymbol{J}) = \sigma_{\max}/\sigma_{\min}, \tag{30}$$

where $\kappa(\boldsymbol{J})$ is the condition number based on the Jacobian matrix, $\sigma_{\max}$ is the square root of the largest eigenvalue

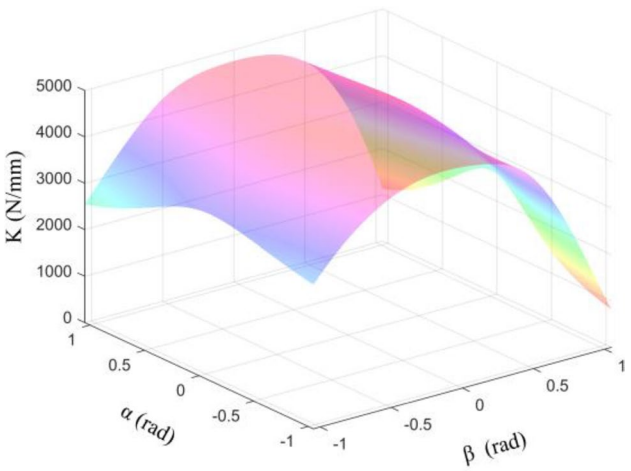

Figure 8 2-UPR-SR parallel upper-limb exoskeleton stiffness distribution

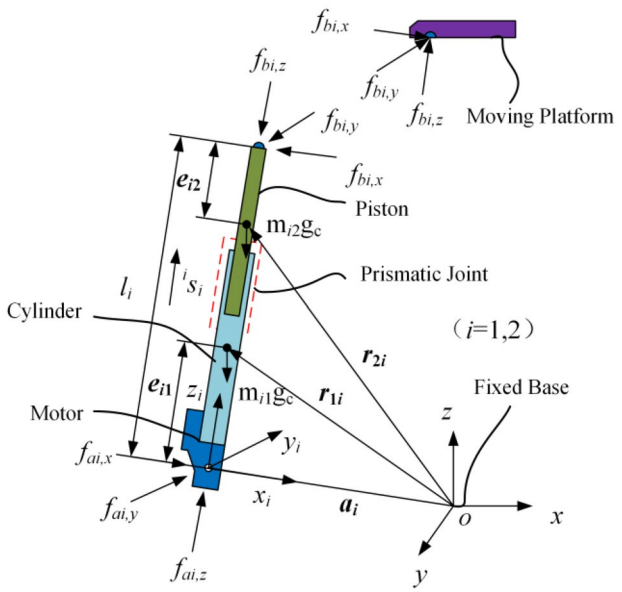

Figure 9 Free body diagram of an actuating limb

in the matrix, and $\sigma_{\min}$ is the square root of the smallest eigenvalue in the matrix.

The dexterity map of the 2-UPR-SR parallel mechanism is symmetrically distributed with rotations around x, which is consistent with the symmetric characteristics of human flexion and extension motions, as shown in Figure 5. For a parallel mechanism, if the condition number does not tend towards infinity, there is no singular position in the mechanism. However, the condition number of the machine in this study is stable, indicating that the mechanism has a stable motion performance and is suitable for the configuration design of human upper-limb exoskeletons. The flexibility of the mechanism is also demonstrated in Figure 6, where the shoulder mismatch is resolved without affecting the flexion movement of the elbow joint, demonstrating a high tolerance to mismatches in the mechanism.

Most conventional shoulder exoskeleton designs are homogeneous; however, owing to the complexity of shoulder joint motion, it is difficult to achieve real-time overlap between the mechanical and biological joints. Instead of making the exoskeleton actively adapt to the motion rhythm of the shoulder joint, thereby increasing the interaction between the shoulder joint and exoskeleton, this study considered the human upper arm as part of the exoskeleton mechanism. Subsequently, the exoskeleton was driven to create a synergistic motion that meets the motion rhythm of the shoulder-humerus from the perspective of human–machine compatibility. Thus, this study discarded the design of the exoskeleton actively adapting to the human body, thereby reducing the interaction between the shoulder joint and the exoskeleton. Consequently, even the presence of a shoulder-humeral rhythm did not affect the movement of the exoskeleton, as shown in Figure 7.

Here, the stiffness is the deformation resistance of the machine when it is subjected to an external load, which reflects the bearing capacity of the mechanism. Since the upper limb augmentation exoskeleton needs to carry heavy objects, the mechanical effect verification of the stiffness characteristics of the parallel mechanism needs to be performed to ensure the safety of task completion. The moving platform of the mechanism is assumed to be subjected to external forces $\boldsymbol{F}_e = [f_e\ n_e]$, and the friction forces at each joint are neglected.

$$K = k\boldsymbol{J}^{\mathrm{T}}\boldsymbol{J}, \tag{31}$$

where $\boldsymbol{F}$ is the external force on the moving platform; $\boldsymbol{K}$ is the stiffness matrix of the mechanism, and k is the equivalent spring constant of the mechanism, where k = 1000 N/mm.

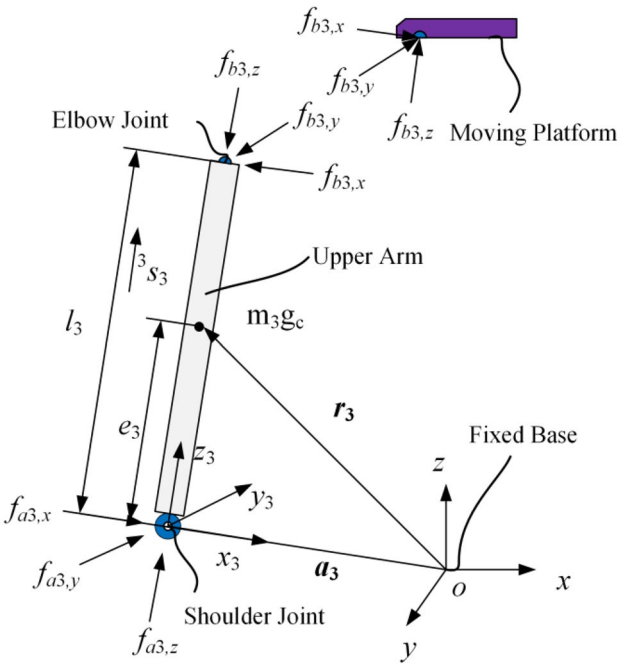

Figure 10 Free body diagram of the passive limb

The enhanced upper-arm exoskeleton must sustain the corresponding concentrated force when carrying heavy objects; therefore, the stiffness of the mechanism must be analyzed and expressed in the form of a minimum eigenvalue distribution, as shown in Figure 8. The maximum stiffness matrix of the 2-UPR-SR parallel mechanism was 4827.20 N/mm, and according to Ref. [40], the maximum concentrated force it can carry is 1376 N. Therefore, the mechanism has a good bearing capacity and can be used to enhance the power assistance of the upper arms.

4 Dynamics Modeling and Analysis

The upper-arm exoskeleton designed in this study is primarily designed to carry objects to enhance the power; therefore, the inverse dynamics problem is that the force at the end of the moving platform is known, and the driving force required by each active limb needs to be determined.

4.1 Active Limb Speed and Acceleration

For analytical convenience, a limb coordinate $o_i - x_i y_i z_i$ system is assumed to be established at the vertex $\boldsymbol{A}_i$ of the fixed platform to represent the posture of each limb about the fixed coordinate system. The active limb and fixed platform cannot rotate around the longitudinal axis because they are connected using a universal joint. The attitude of the limb coordinate system relative to the fixed coordinate system is represented using two Euler angles, which rotate α_i around the axis x_i and β_i

around the axis y_i. Therefore, the rotation matrix of the limbed coordinate system relative to the fixed coordinate system was given by

$$\boldsymbol{R}_I^A = \begin{bmatrix} \cos\beta_i & \sin\beta_i \sin\alpha_i & \sin\beta_i \cos\alpha_i \\ 0 & \cos\alpha_i & -\sin\alpha_i \\ -\sin\beta_i & \cos\beta_i \sin\alpha_i & \cos\beta_i \cos\alpha_i \end{bmatrix}. \tag{32}$$

As shown in Figure 9, each active limb includes a cylinder and piston. Among them, e_{i1} is the distance between the point A_i and the center of mass of the lower rod, and e_{i2} is the distance between the point B_i and the center of mass of the upper rod. Therefore, the center of mass of the upper and lower rod limbs in the limb can be expressed as:

$$\begin{cases} \boldsymbol{r}_{1i} = \boldsymbol{a}_i + e_{i1}\boldsymbol{s}_i, \\ \boldsymbol{r}_{2i} = \boldsymbol{a}_i + (l_i - e_{i1})\boldsymbol{s}_i, \end{cases} \tag{33}$$

and the vector closed-loop equation of the limbed chain can be given by

$$\boldsymbol{a}_i + l_i\boldsymbol{s}_i = \boldsymbol{p} + \boldsymbol{b}_i. \tag{34}$$

The linear and angular velocities of each limb were calculated according to the velocity and angular velocity of the moving platform, which can be obtained via derivation with respect to the time based on the right side of Eq. (34).

$$\boldsymbol{v}_{bi} = \boldsymbol{v}_p + \boldsymbol{\omega}_p \times \boldsymbol{b}_i, \tag{35}$$

where $\boldsymbol{v}_{bi}$ is the velocity of the endpoint B_i of the moving platform in a fixed coordinate system. Using this derivative, the conversion of $\boldsymbol{v}_{bi}$ to the limbed-chain coordinate system can be expressed as

$${}^i\boldsymbol{v}_{bi} = {}^i\boldsymbol{R}_A\boldsymbol{v}_{bi} = l_i^i\boldsymbol{\omega}_i \times {}^i\boldsymbol{s}_i + \dot{l}_i^i\boldsymbol{s}_i, \tag{36}$$

where ${}^i\boldsymbol{v}_{bi} = \begin{bmatrix} {}^i\boldsymbol{v}_{bix} & {}^i\boldsymbol{v}_{biy} & {}^i\boldsymbol{v}_{biz} \end{bmatrix}^{\mathrm{T}}$.

Multiplying both sides of Eq. (36) by ${}^i\boldsymbol{s}_i$, we obtain

$$\dot{l}_i = {}^i\boldsymbol{s}_i^i\boldsymbol{v}_{bi} = {}^i\boldsymbol{v}_{biz}. \tag{37}$$

For Eq. (36), ${}^i\boldsymbol{s}_i$ was forked and multiplied on both sides since the active limb cannot rotate around the longitudinal axis; subsequently, $\boldsymbol{\omega}_i^{\mathrm{T}}\boldsymbol{s}_i = 0$ and

$${}^i\boldsymbol{\omega}_i = \frac{1}{l_i}({}^i\boldsymbol{s}_i \times {}^i\boldsymbol{v}_{bi}) = \frac{1}{l_i}\begin{bmatrix} -{}^i\boldsymbol{v}_{biy} \\ {}^i\boldsymbol{v}_{bix} \\ 0 \end{bmatrix}. \tag{38}$$

After the angular velocity of the limb was obtained, the centroid velocities of the sleeve and piston were derived using Eq. (34) with respect to time.

$${}^i\boldsymbol{v}_{i1} = e_{i1}^i\boldsymbol{\omega}_i \times {}^i\boldsymbol{s}_i = \frac{e}{l_i}\begin{bmatrix} {}^i\boldsymbol{v}_{bix} \\ {}^i\boldsymbol{v}_{biy} \\ 0 \end{bmatrix}, \tag{39}$$

$${}^i\boldsymbol{v}_{i2} = (l_i - e_{i2})^i\boldsymbol{\omega}_i \times {}^i\boldsymbol{s}_i + \dot{l}_i^i\boldsymbol{s}_i = \frac{1}{l_i}\begin{bmatrix} (l_i - e_{i2})^i\boldsymbol{v}_{bix} \\ (l_i - e_{i2})^i\boldsymbol{v}_{biy} \\ l_i^i\boldsymbol{v}_{biz} \end{bmatrix}. \tag{40}$$

The linear acceleration of the cylinder and center of mass of the piston were then obtained via derivation using Eqs. (39) and (40) with respect to time.

$${}^i\boldsymbol{a}_{i1} = e_{i1}^i\dot{\boldsymbol{\omega}}_i \times {}^i\boldsymbol{s}_i + e_{i1}^i\boldsymbol{\omega}_i \times ({}^i\boldsymbol{\omega}_i \times {}^i\boldsymbol{s}_i), \tag{41}$$

$$\begin{aligned} {}^i\boldsymbol{a}_{i2} = {} & \ddot{l}_i^i\boldsymbol{s}_i + (l_i - e_{i2})^i\dot{\boldsymbol{\omega}}_i \times {}^i\boldsymbol{s}_i + (l_i - e_{i2})^i\boldsymbol{\omega}_i \\ & \times ({}^i\boldsymbol{\omega}_i \times {}^i\boldsymbol{s}_i) + 2\dot{l}_i^i\boldsymbol{\omega}_i \times {}^i\boldsymbol{s}_i. \end{aligned} \tag{42}$$

4.2 Upper Arm Passive Limb Velocity and Acceleration

As shown in Figure 10, e_3 is the distance between point A_3 and the center of mass of the passive limb, which can be expressed as

$$\boldsymbol{r}_3 = \boldsymbol{a}_3 + e_3\boldsymbol{s}_3. \tag{43}$$

Additionally, the vector closed-loop equation of the limbed chain can be obtained as

$$\boldsymbol{a}_3 + l_3\boldsymbol{s}_3 = \boldsymbol{p} + \boldsymbol{b}_3. \tag{44}$$

Subsequently, the linear and angular velocities of the passive limb were calculated according to the velocity and angular velocity of the moving platform, which can be obtained via derivation with respect to the time using the right side of Eq. (44).

$$\boldsymbol{v}_{b3} = \boldsymbol{v}_p + \boldsymbol{\omega}_p \times \boldsymbol{b}_3, \tag{45}$$

where $\boldsymbol{v}_3$ is the velocity of the endpoint B_3 of the moving platform in a fixed coordinate system.

Using this derived value, $\boldsymbol{v}_3$ can be converted into the limbed coordinate system based on Eq. (46). Therefore,

$${}^3\boldsymbol{v}_{b3} = {}^3R_A\boldsymbol{v}_{b3} = l_3^3\boldsymbol{\omega}_3 \times {}^3\boldsymbol{s}_3 + \dot{l}_3^3\boldsymbol{s}_3, \tag{46}$$

where ${}^3\boldsymbol{v}_{b3} = \begin{bmatrix} {}^3\boldsymbol{v}_{b3x} & {}^3\boldsymbol{v}_{b3y} & {}^3\boldsymbol{v}_{b3z} \end{bmatrix}^{\mathrm{T}}$.

Subsequently, ${}^3\boldsymbol{s}_3$ is forked and multiplied on both sides of Eq. (46) because the active limb cannot rotate around the longitudinal axis (note that the inner and outer rotations of the upper arm are not considered here). This causes $\boldsymbol{\omega}_3^{\mathrm{T}}\boldsymbol{s}_3 = 0$, which is calculated as

$$^3\boldsymbol{\omega}_3 = \frac{1}{l_3}(^3\boldsymbol{s}_3 \times {}^3\boldsymbol{v}_{b3}) = \frac{1}{l_3}\begin{bmatrix} -^3v_{b3y} \\ -^3v_{b3x} \\ 0 \end{bmatrix}. \tag{47}$$

Once the angular velocity of the limb is obtained, the centroid velocity of the passive limb can be obtained via derivation using Eq. (43) with respect to time:

$$^3\boldsymbol{v}_3 = e_3^3\boldsymbol{\omega}_3 \times {}^3\boldsymbol{s}_3 = \frac{e_3}{l_3}\begin{bmatrix} ^3v_{b3x} \\ ^3v_{b3y} \\ 0 \end{bmatrix}, \tag{48}$$

where $^3\boldsymbol{v}_3$ represents the velocity of the center of mass of the passive limb in the limb coordinate system.

The acceleration of the endpoint B_3 of the moving platform is then obtained via derivation using Eq. (45) with respect to time.

$$\dot{\boldsymbol{v}}_{b3} = \dot{\boldsymbol{v}}_p + \dot{\boldsymbol{\omega}}_p \times \boldsymbol{b}_3 + \boldsymbol{\omega}_p \times (\boldsymbol{\omega}_p \times \boldsymbol{b}_3). \tag{49}$$

Based on this derived value, the following expression holds:

$$\begin{aligned} ^3\boldsymbol{a}_{b3} =& ^3\dot{\boldsymbol{v}}_{b3} = {}^3\boldsymbol{R}_A\dot{\boldsymbol{v}}_{b3} = l_3^3\dot{\boldsymbol{\omega}}_3 \times {}^3\boldsymbol{s}_3 \\ &+ l_3^3\boldsymbol{\omega}_3 \times (^3\boldsymbol{\omega}_3 \times {}^3\boldsymbol{s}_3). \end{aligned} \tag{50}$$

Subsequently, by simultaneously cross-multiplying $^3\boldsymbol{s}_3$ on both sides of Eq. (50), we obtain

$$^3\dot{\boldsymbol{\omega}}_3 = \frac{1}{l_3}{}^3\boldsymbol{s}_3 \times {}^3\dot{\boldsymbol{v}}_{bi3} = \frac{1}{l_i}\begin{bmatrix} ^i\dot{\boldsymbol{v}}_{biy} \\ ^i\dot{\boldsymbol{v}}_{bix} \\ 0 \end{bmatrix}. \tag{51}$$

The linear acceleration of the center of mass of the passive limb can also be obtained via derivation using Eq. (48) with respect to time.

$$^3\boldsymbol{a}_3 = e_3^3\dot{\boldsymbol{\omega}}_3 \times {}^3\boldsymbol{s}_3 + e_3^3\boldsymbol{\omega}_3 \times (^3\boldsymbol{\omega}_3 \times {}^3\boldsymbol{s}_3) = \frac{e_3}{l_3}\begin{bmatrix} ^3\dot{\boldsymbol{v}}_{b3x} \\ ^3\dot{\boldsymbol{v}}_{b3y} \\ -\frac{^3v_{b3x}^2 + {}^3v_{b3y}^2}{l_3} \end{bmatrix}. \tag{52}$$

4.3 Dynamic Equation Based on the Jacobian Matrix

Eq. (35) was written in the matrix form to simplify the limbed Jacobian matrix of the parallel mechanism to:

$$\boldsymbol{v}_{bi} = \boldsymbol{J}_{bi}\dot{\boldsymbol{x}}_p, \tag{53}$$

where,

$$\boldsymbol{J}_{bi} = \begin{bmatrix} 1 & 0 & 0 & 0 & b_{iz} & -b_{iy} \\ 0 & 1 & 0 & -b_{iz} & 0 & b_{ix} \\ 0 & 0 & 1 & b_{iy} & -b_{ix} & 0 \end{bmatrix},$$

Table 2 Dynamic simulation parameters

Attributes	Value
Moving platform quality m_p(kg)	0.24
Upper arm chain quality m_3(kg)	1.95
Cylinder quality m_{i1}(kg)	1.03
Piston quality m_{i2}(kg)	0.3
Upper arm centroid distance e_3(mm)	160
Cylinder centroid distance e_2(mm)	80
Piston centroid distance e_1(mm)	80

and $\dot{\boldsymbol{x}}_p = \begin{bmatrix} v_{px} & v_{py} & v_{pz} & w_{px} & w_{py} & w_{pz} \end{bmatrix}^{\mathrm{T}}$ indicate the linear and angular velocities of the moving platform.

Eq. (53) can be converted to the limbed-chain coordinate system as

$$^i\boldsymbol{v}_{bi} = {}^i\boldsymbol{J}_{bi}\dot{\boldsymbol{x}}_p = \begin{bmatrix} ^i\boldsymbol{J}_{bix} \\ ^i\boldsymbol{J}_{biy} \\ ^i\boldsymbol{J}_{biz} \end{bmatrix}\dot{\boldsymbol{x}}_p, \tag{54}$$

and using the properties of Eq. (54), Eq. (37) can be rewritten as follows:

$$\dot{l}_i = {}^i\boldsymbol{v}_{biz} = {}^i\boldsymbol{J}_{\mathrm{biz}}\dot{\boldsymbol{x}}_p. \tag{55}$$

Because there is no linear displacement of the passive limb along the longitudinal axis, the Jacobian matrix of the two driving limbs can be written twice based on Eq. (55) as

$$\begin{bmatrix} \dot{l}_1 \\ \dot{l}_2 \\ 0 \\ 0 \\ 0 \\ 0 \end{bmatrix} = \boldsymbol{J}_p\dot{\boldsymbol{x}}_p, \tag{56}$$

where $\boldsymbol{J}_p = \begin{bmatrix} ^1\boldsymbol{J}_{b1z} \\ ^2\boldsymbol{J}_{b2z} \\ 0_{1\times6} \\ 0_{1\times6} \\ 0_{1\times6} \\ 0_{1\times6} \end{bmatrix}_{0\times6}$ is the Jacobian of the parallel mechanism.

For the active limb, Eqs. (38)–(40) were similarly transformed using Eq. (54) to obtain

$$^i\dot{\boldsymbol{x}}_{i1} = {}^i\boldsymbol{J}_{i1}\dot{\boldsymbol{x}}_p, \tag{57}$$

$$^i\dot{\boldsymbol{x}}_{i2} = {}^i\boldsymbol{J}_{i2}\dot{\boldsymbol{x}}_p, \tag{58}$$

where $^i\dot{\boldsymbol{x}}_{i1}$ and $^i\dot{\boldsymbol{x}}_{i2}$ represent the velocities of the center of mass of the upper and lower rods of the i-th active limb, respectively. $^i\boldsymbol{J}_{i1}$ and $^i\boldsymbol{J}_{i2}$ are the link Jacobian matrices,

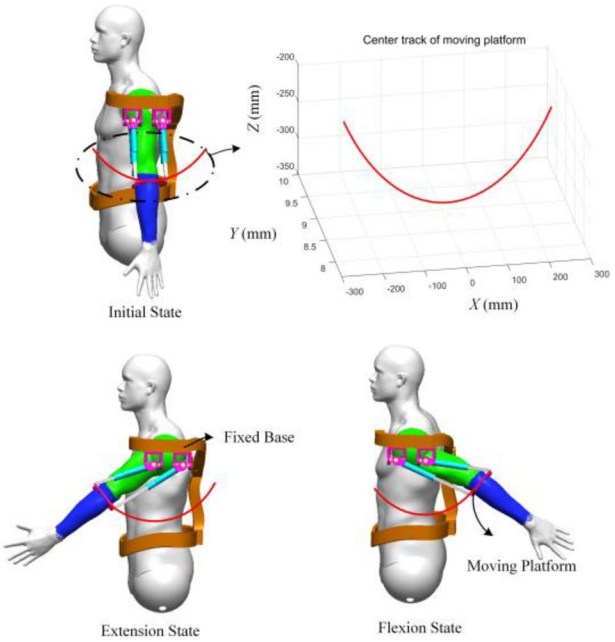

Figure 11 Flexion and extension motions

respectively, of the cylinder and positon in the i-th active limb.

$$\begin{cases} {}^{i}\boldsymbol{J}_{i1} = \dfrac{1}{l_i}\begin{bmatrix} e_1{}^{i}\boldsymbol{J}_{bix} \\ e_1{}^{i}\boldsymbol{J}_{biy} \\ \boldsymbol{0}_{1\times 6} \\ -{}^{i}\boldsymbol{J}_{biy} \\ {}^{i}\boldsymbol{J}_{bix} \\ \boldsymbol{0}_{1\times 6} \end{bmatrix}, \\ {}^{i}\boldsymbol{J}_{i2} = \dfrac{1}{l_i}\begin{bmatrix} (l_i - e_2){}^{i}\boldsymbol{J}_{bix} \\ (l_i - e_2){}^{i}\boldsymbol{J}_{biy} \\ l_i{}^{i}\boldsymbol{J}_{biz} \\ -{}^{i}\boldsymbol{J}_{biy} \\ {}^{i}\boldsymbol{J}_{bix} \\ \boldsymbol{0}_{1\times 6} \end{bmatrix}. \end{cases}$$

Similarly, for the passive limb, Eq. (54) was used to rewrite Eqs. (47) and (48) as

$${}^{3}\boldsymbol{w}_3 = \frac{1}{l_3}\begin{bmatrix} -{}^{3}\boldsymbol{J}_{b3y} \\ -{}^{3}\boldsymbol{J}_{b3x} \\ \boldsymbol{0}_{1\times 6} \end{bmatrix}\dot{\boldsymbol{x}}_p, \tag{59}$$

$${}^{3}\boldsymbol{v}_3 = \frac{1}{l_3}\begin{bmatrix} {}^{3}\boldsymbol{J}_{b3x} \\ {}^{3}\boldsymbol{J}_{b3y} \\ \boldsymbol{0}_{1\times 6} \end{bmatrix}\dot{\boldsymbol{x}}_p. \tag{60}$$

Subsequently,

$${}^{3}\dot{\boldsymbol{x}}_3 = {}^{3}\boldsymbol{J}_3\dot{\boldsymbol{x}}_p. \tag{61}$$

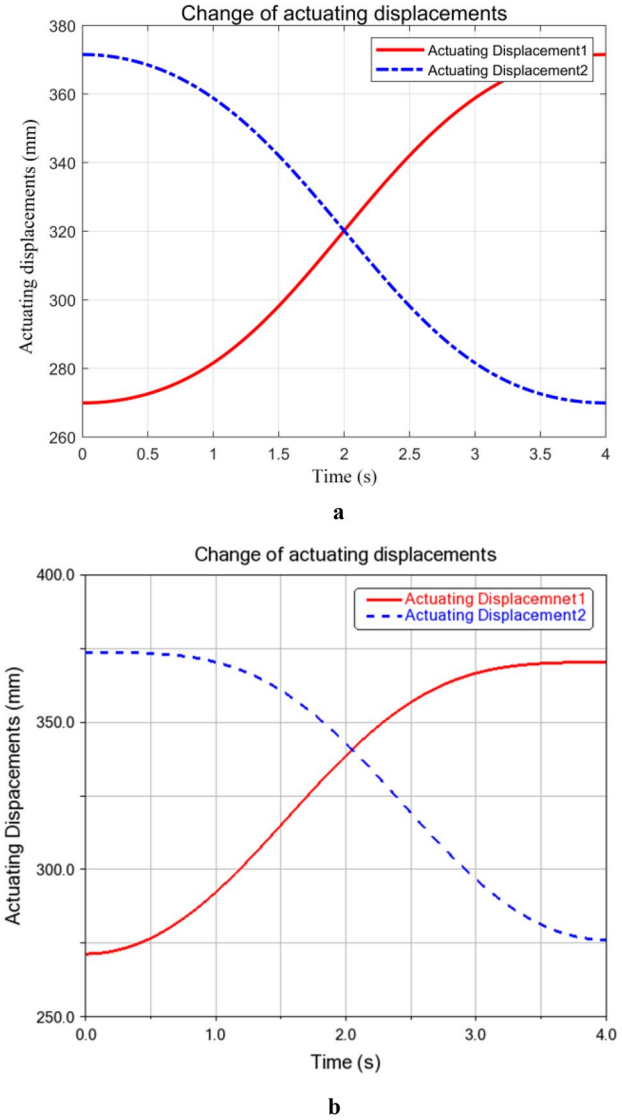

Figure 12 One cycle of actuating displacements: actuating displacements using **a** MATLAB and **b** ADAMS

Assuming that the resultant force vector of the moving 2-UPR-SR parallel mechanism platform is $\boldsymbol{F}_{\mathrm{e}} = \begin{bmatrix} \boldsymbol{f}_{\mathrm{e}} & \boldsymbol{n}_{\mathrm{e}} \end{bmatrix}^{\mathrm{T}}$,

$$\boldsymbol{F}_p = \begin{bmatrix} \boldsymbol{f}_p \\ \boldsymbol{n}_p \end{bmatrix} = \begin{bmatrix} \boldsymbol{f}_{\mathrm{e}} + \mathrm{m}_p\boldsymbol{g} - \mathrm{m}_p\boldsymbol{a}_p \\ \boldsymbol{n}_{\mathrm{e}} - {}^{A}\boldsymbol{I}_p\dot{\boldsymbol{\omega}}_p - \boldsymbol{\omega}_p \times \left({}^{A}\boldsymbol{I}_p\boldsymbol{\omega}_p\right) \end{bmatrix}, \tag{62}$$

where $\boldsymbol{F}_p$ represents the resultant force vector received by the center of mass of the moving platform, m_p represents the mass of the moving platform, ${}^{A}\boldsymbol{I}_p$ represents the inertial moment of the moving platform about the fixed frame, where ${}^{A}\boldsymbol{I}_p = {}^{A}\boldsymbol{R}_B{}^{B}\boldsymbol{I}_P^{B}\boldsymbol{R}_A$, and ${}^{B}\boldsymbol{I}_p$ represents the

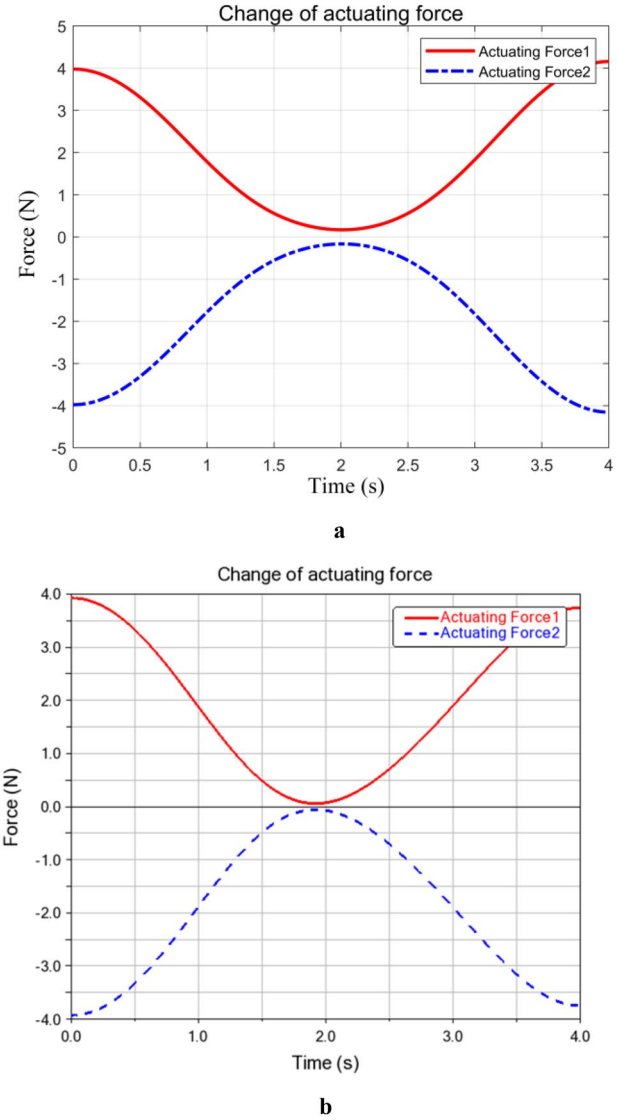

Figure 13 One cycle of actuating forces: actuating forces using **a** MATLAB and **b** ADAMS

inertial moment of the moving platform about the moving coordinate system.

For the two parallel mechanism drive limbs, the resultant force vectors are ${}^{i}\boldsymbol{F}_{il} = \left[{}^{i}f_{i1}, {}^{i}n_{i1}\right]$ and ${}^{i}\boldsymbol{F}_{i2} = \left[{}^{i}f_{i2}, {}^{i}n_{i2}\right]$.

$$ {}^{i}\boldsymbol{F}_{i1} = \begin{bmatrix} \mathrm{m}_{i1}{}^{i}\boldsymbol{R}_{A}\boldsymbol{g} - \mathrm{m}_{i1}^{i}\boldsymbol{a}_{i1} \\ -{}^{i}\boldsymbol{I}_{i1}^{i}\dot{\boldsymbol{\omega}}_{i} - {}^{i}\boldsymbol{\omega}_{i} \times \left({}^{i}\boldsymbol{I}_{i1}^{i}\boldsymbol{\omega}_{i}\right) \end{bmatrix}, \tag{63} $$

$$ {}^{i}\boldsymbol{F}_{i2} = \begin{bmatrix} \mathrm{m}_{i2}{}^{i}\boldsymbol{R}_{A}\boldsymbol{g} - \mathrm{m}_{i2}^{i}\boldsymbol{a}_{i2} \\ -{}^{i}\boldsymbol{I}_{i2}^{i}\dot{\boldsymbol{\omega}}_{i} - {}^{i}\boldsymbol{\omega}_{i} \times \left({}^{i}\boldsymbol{I}_{i2}^{i}\boldsymbol{\omega}_{i}\right) \end{bmatrix}. \tag{64} $$

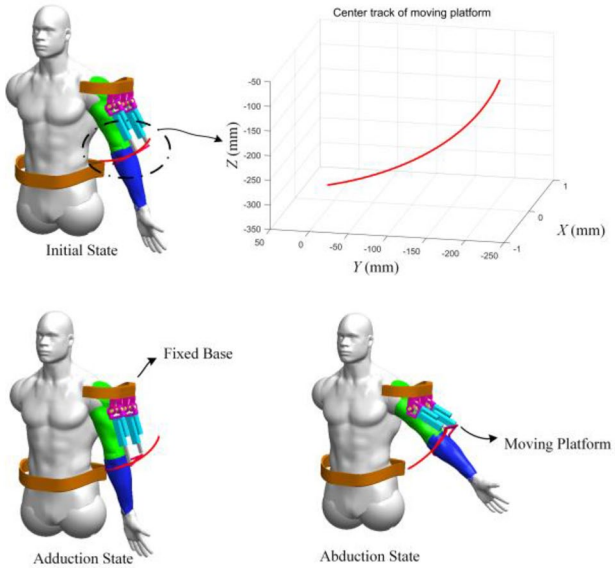

Figure 14 Abduction and adduction motions

In the equation, ${}^{i}\boldsymbol{F}_{i1}$ and ${}^{i}\boldsymbol{F}_{i2}$ are the resultant force vectors between the lower and upper rods of the limb, m_{i1} and m_{i2} are the masses of the lower and upper rods of the limb, respectively, and ${}^{i}\boldsymbol{I}_{i1}$ and ${}^{i}\boldsymbol{I}_{i2}$ are the inertia of the lower and upper rods of the limb, respectively.

For the passive limb resultant force vector ${}^{3}\boldsymbol{F}_{3} = [{}^{3}f_{3}, {}^{3}n_{3}]$ of the parallel structure:

$$ {}^{3}\boldsymbol{F}_{3} = \begin{bmatrix} \mathrm{m}_{3}^{3}\boldsymbol{R}_{A}\boldsymbol{g} - \mathrm{m}_{3}{}^{3}\boldsymbol{a}_{3} \\ -{}^{3}\boldsymbol{I}_{3}^{3}\dot{\boldsymbol{\omega}}_{3} - {}^{3}\boldsymbol{\omega}_{3} \times \left({}^{3}\boldsymbol{I}_{3}{}^{3}\boldsymbol{\omega}_{3}\right) \end{bmatrix}, \tag{65} $$

where ${}^{3}\boldsymbol{F}_{3}$ is the resultant force vector in the passive limb, m_{3} is the mass of the passive limb, ${}^{3}\boldsymbol{I}_{3}$ is the inertial moment of the passive limb, and the superscript 3 indicates the passive limb coordinate system.

The dynamic equation of the 2-UPR-SR parallel mechanism was derived using the principle of virtual work, as follows:

$$ \boldsymbol{J}_{p}^{\mathrm{T}}\boldsymbol{\tau} + \boldsymbol{F}_{p} + \sum_{i=1}^{2}\left({}^{i}\boldsymbol{J}_{i1}^{\mathrm{T}i}\boldsymbol{F}_{i1} + {}^{i}\boldsymbol{J}_{i2}^{\mathrm{T}i}\boldsymbol{F}_{i2}\right) + {}^{3}\boldsymbol{J}_{3}^{\mathrm{T}3}\boldsymbol{F}_{3} = 0, \tag{66} $$

where $\boldsymbol{\tau} = \begin{bmatrix} \tau_1 & \tau_2 \end{bmatrix}$ denotes the driving force required by the two active limbs. It is worth noting that $\boldsymbol{F}_{p}$ is represented in the fixed frame A, ${}^{i}\boldsymbol{F}_{i1}$ and ${}^{i}\boldsymbol{F}_{i2}$ are respectively transformed in the fixed coordinate system using the limbed Jacobian matrices ${}^{i}\boldsymbol{J}_{i1}$ and ${}^{i}\boldsymbol{J}_{i2}$, and the driving force $\boldsymbol{\tau}$ is transformed in the fixed coordinate system using the parallel mechanism Jacobian matrix $\boldsymbol{J}_{p}$ middle. The dynamic problem of the 2-UPR-SR mechanism was

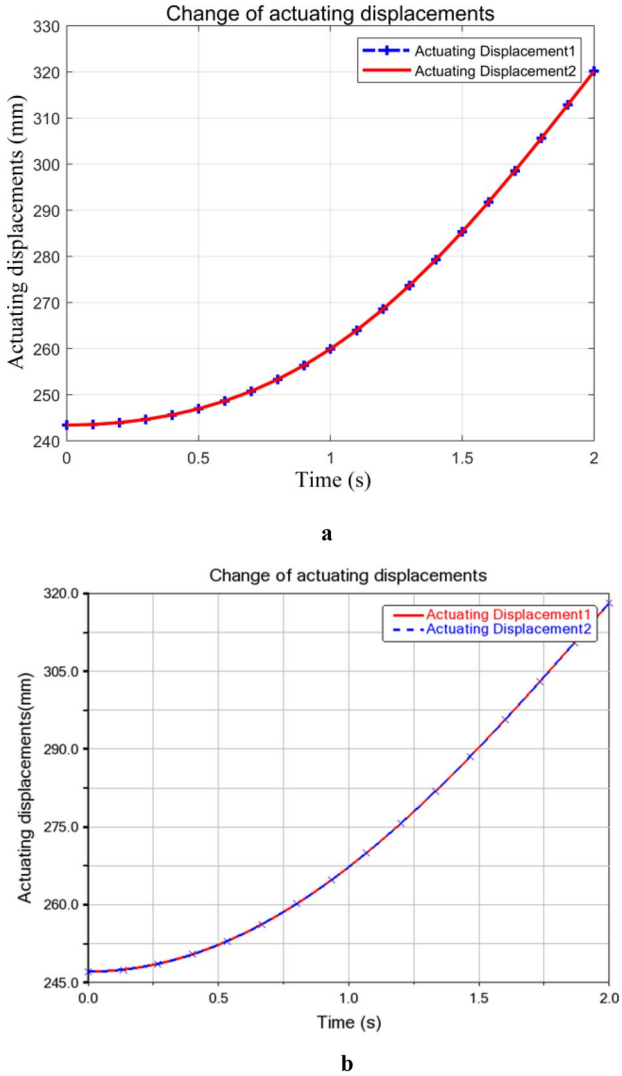

Figure 15 One cycle of actuating displacements: actuating displacements using the **a** MATLAB and **b** ADAMS

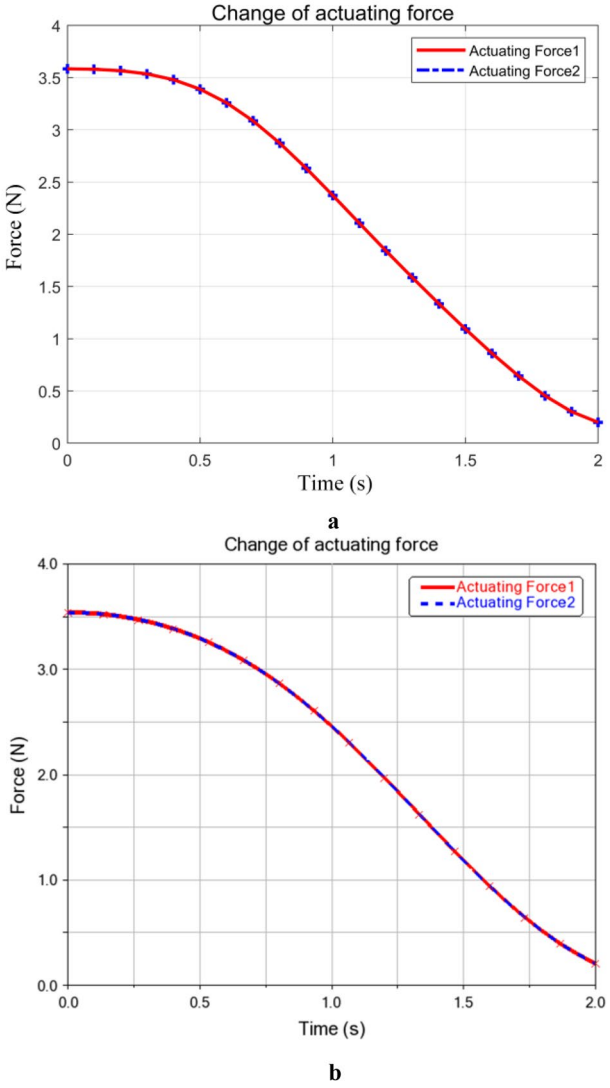

Figure 16 One cycle of actuating forces: actuating forces using **a** MATLAB and **b** ADAMS

theoretically calculated and verified using a simulation method with the parameters listed in Table 2.

5 Human–machine Modeling Simulation and Case Analysis

5.1 Human–machine Modeling and Simulation

Compared with the lower limbs of the human body, the upper limbs of the human body have no regular movements such as gait. Therefore, the upper limb flexion and extension angles α, and adduction and abduction angles β were defined. At $\beta = 0$ and $\alpha = 0.9 \times \cos(\pi/4 \times t)$, the moving platform rotates around the x-axis, that is, the flexion and extension of the upper-limb exoskeleton, as shown in Figure 11. The red curve in Figure 11 represents the trajectory of the center of the moving platform during flexion and extension. The corresponding changes in the driving displacement and driving force are shown in Figures 12 and 13, respectively. At $\beta = 0.9 \times \cos(\pi/4 \times t)$ and $\alpha = 0$, the moving platform rotates around the y-axis, that is, the adduction and abduction movements of the upper-limb exoskeleton, as shown in Figure 14. The red curve in the figure represents the trajectory of the center of the moving platform during abduction and adduction, and the corresponding changes in the driving displacement and driving force are shown in Figures 15 and 16, respectively.

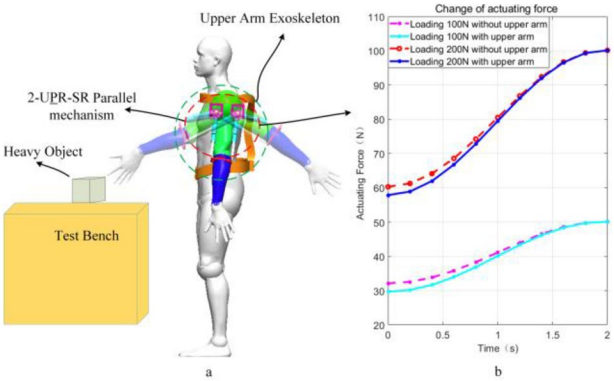

Figure 17 Flexion and extension force distributions when picking up and placing down heavy objects: **a** diagram of the flexion and extension used to pick up and place down objects, and **b** change in the actuating force

As previously mentioned, the two driving limbs are symmetrically distributed in the sagittal plane of the body. When the mechanism performs the flexion and extension movements of the human body, the mobile pair performs the extension or contraction movement, respectively, and the driving force in the two active limbs changes under the same amplitude and in the opposite direction, which is in line with the actual force during flexion and extension. When the mechanism performs adduction and abduction motions, the moving pairs simultaneously perform elongation or contraction motions, and the driving force change in the two active limbs are the same, which is consistent with the actual force conditions during adduction and abduction. Moreover, the consistency in the theoretical and simulation values validates the kinematic and dynamic modeling of the 2-UPR-SR parallel upper-limb exoskeleton. As shown in Figures 13 and 16, the theoretical and simulated values are relatively smooth at the peak values, indicating that the parallel mechanism has a better dynamic performance during this movement and can be used to enhance the power assistance of the upper arms.

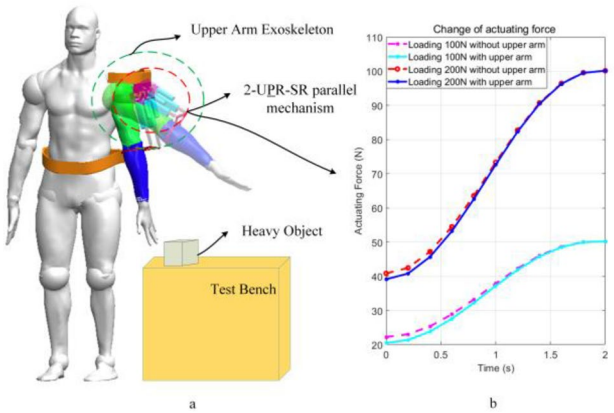

Figure 18 Abduction and adduction when picking up and placing down heavy objects: **a** diagram of flexion and extension when picking up and placing down objects, and **b** change in the actuating force.

5.2 Case Analysis

To achieve effective upper-limb augmentation assistance, this section presents a case study involving the lifting of a heavy object with one arm. As shown in Figure 17a, after the human body is fitted with an exoskeleton, the heavy objects are picked up using a flexion motion and placed down using a stretching motion. As shown in Figure 18a, the human body lifts heavy objects through abduction when wearing an exoskeleton. Throughout this process, the upper limbs of the body only follow the movement and are not the main bearers of the driving force, and the sleeve motor in the two-drive limb enables heavy objects to be transported by changing the thrust of the piston rod.

Figure 17b shows the shift in the driving force for the two active limbs with different loads during flexion and extension, and Figure 18b shows the shift in the driving force for the two active limbs with different loads during the adduction and abduction processes. A comparison of Figures 17b and 18b shows that the initial values of the driving force are different when lifting the same weight owing to the different ranges of body motions in the flexion-extension and abduction-adduction degrees of freedom, which in turn leads to different initial boosts of the active strut. However, the push and pull forces were not proportional to the loading forces, reflecting the complex dynamic behavior of the upper-limb exoskeleton. Notably, the results of the comparative simulations with and without upper-arm involvement show that during the initial phase of movement, the upper arm reduces the need for actuation forces, indicating that the upper arm plays

a coordinating role during movement, reflecting high human–machine compatibility. As the movement progressed, the boost role of the upper arm diminished and was entirely taken up by the drive support chain, causing no burden on the body.

6 Conclusions

In this study, a parallel shoulder exoskeleton was designed using the human upper arm as a passive support chain to solve the shoulder-joint mismatch problem during assistance. The following conclusions were drawn.

(1) The shoulder joint parallel exoskeleton satisfies the two degrees of freedom of human flexion/extension and internal abduction/adduction motions, and its working space satisfies the requirements for carrying heavy objects.
(2) The 2-UPR-SR parallel mechanism can withstand a load of at least 1376 N. The dexterity mapping show that using the human body as the passive support chain mechanism of a parallel mechanism can improve human–machine compatibility and is an effective design method for solving the shoulder-joint mismatch problem.
(3) Human–machine dynamics model can be developed using the principle of virtual work, and the high consistency between the theoretical and simulated values demonstrates the accuracy of the human–machine modeling approach.
(4) The human upper arm effectively participates in the synergistic movement of the upper limb and reduces the driving force demand at the initial stage of assistance, thereby achieving good human–machine compatibility. This is evident from the simulation results of the heavy lifting case.

Acknowledgements
Not applicable.

Author contributions
LN wrote the manuscript; SG, MS, YW and QH assisted with sampling and laboratory analyses. All authors read and approved the final manuscript.

Authors' Information
Lianzheng Niu, born in 1994, is currently a Ph.D. candidate at *Robotics Research Center, Beijing Jiaotong University, China*. He received his Bachelor's degree from *Henan University of Engineering, China,* in 2018. In 2021, he received his Master's degree from *North China University of Technology, China*. His research interests include robotic mechanisms and exoskeleton–parallel robots.
E-mail: lianzheng_niu@bjtu.edu.cn
Sheng Guo, born in 1972, received his Ph.D. from *Beijing Jiaotong University, China,* in 2005. He was a Visiting Scholar at *University of California, Irvine, US*, in 2010–2011. Currently, he is a Full Professor, the Vice Director of the Robotics Institute, and the Dean of *School of Mechanical, Electronic and Control Engineering, Beijing Jiaotong University, China*. His research interests include robotic mechanisms and mechatronics.
E-mail: shguo@bjtu.edu.cn
Majun Song, born in 1990, is currently a Ph.D. candidate at the *School of Mechanical, Electronic and Control Engineering, Beijing Jiaotong University, China*. He is also a joint Ph.D. student in the biomechanics group, *Department of Materials and Production, Aalborg University, Denmark*. He received his Master's degree from the *Jiangxi University of Science and Technology, China*, in 2016. His research interests include parallel robots, robotic prostheses, human–machine modeling, and biomechanics.
E-mail: 18116021@bjtu.edu.cn
Yifan Wu, born in 1993, is currently a Ph.D. candidate at the *Robotics Research Center, Beijing Jiaotong University, China*. He received his Bachelor's degree from the *Beijing Jiaotong University, China,* in 2016. In 2019, he received a Diploma in Engineering and Master's degree from the *University of Montpellier, France*. His research interests include control methods for legged robots, machine learning, and innovation of parallel mechanisms.
E-mail: yifanwu@bjtu.edu.cn
Haibo Qu, born in 1983, is currently a Lecturer at *the Robotics Institute, Beijing Jiaotong University, China*. He received his Ph.D. from the *Beijing Jiaotong University, China,* in 2013. His research interests include robotic mechanisms and mechanical design.
E-mail: hbqu@bjtu.edu.cn

Funding
Supported by National Natural Science Foundation of China (Grant No. 52275004).

Availability of data and materials
The datasets supporting the conclusions of this article are included within the article.

Declarations

Competing interests
The authors declare no competing financial interests.

Received: 29 September 2022 Revised: 27 March 2023 Accepted: 3 April 2023
Published online: 16 May 2023

References

[1] R Bogue. Exoskeletons: a review of recent progress. *Industrial Robot-the International Journal of Robotics Research and Application*, 2022, 49(5): 813–818.
[2] C Liu, C Zhu, H B Liang, et al. Development of a light wearable exoskeleton for upper extremity augmentation. *23rd International Conference on Mechatronics and Machine Vision in Practice*, Nanjing, China, November 28–30, 2016: 323–328.
[3] D B Sui, J Z Fan, H Z Jin, et al. Design of a wearable upper-limb exoskeleton for activities assistance of daily living. *IEEE International Conference on Advanced Intelligent Mechatronics*, Munich, Germany, July 3–7, 2017: 845–850.
[4] R Gopura, D S V Bandara, K Kiguchi, et al. Developments in hardware systems of active upper-limb exoskeleton robots: A review. *Robotics and Autonomous Systems*, 2016, 75: 203–220.
[5] J Huang, X K Tu, J P He. Design and evaluation of the RUPERT wearable upper extremity exoskeleton robot for clinical and in-home therapies. *IEEE Transactions on Systems Man Cybernetics-Systems*, 2016, 46(7): 926–935.
[6] J Lenarcic, M Stanisic. A humanoid shoulder complex and the humeral pointing kinematics. *IEEE Transactions on Robotics & Automation*, 2003, 19(3): 499–506.
[7] G Wu, S Siegler, P Allard, et al. ISB recommendation on definitions of joint coordinate system of various joints for the reporting of human joint motion--part I: ankle, hip, and spine. *International Society of Biomechanics. Journal of Biomechanics*, 2002, 35(4): 543–548.
[8] P Herbin, M Pajor. Human-robot cooperative control system based on serial elastic actuator bowden cable drive in ExoArm 7-DOF upper

extremity exoskeleton. *Mechanism and Machine Theory*, 2021, 163: 104372.
[9] P Elvira, C Martina, M Simone, et al. Evaluation of the effects of the Arm Light Exoskeleton on movement execution and muscle activities: a pilot study on healthy subjects. *Journal of Neuro Engineering and Rehabilitation*, 2016, 13(9): 1–21.
[10] R J Farris, H A Quintero, M Goldfarb. Preliminary evaluation of a powered lower limb orthosis to aid walking in paraplegic individuals. *IEEE Transactions on Neural Systems and Rehabilitation Engineering*, 2011, 19(6): 652–659.
[11] A Esquenazi, M Talaty, A Packel, et al. The ReWalk powered exoskeleton to restore ambulatory function to individuals with thoracic-level motor-complete spinal cord injury. *American Journal of Physical Medicine & Rehabilitation*, 2012, 91(11): 911–921.
[12] Y Lee, B Choi, J Lee, et al. Flexible sliding frame for gait enhancing mechatronic system (GEMS). *38th Annual International Conference of the IEEE Engineering in Medicine and Biology Society*, Orlando, USA, August 16–20, 2016: 598–602.
[13] A H A Stienen, E E G Hekman, F C T Helm, et al. Self-aligning exoskeleton axes through decoupling of joint rotations and translations. *IEEE Transactions on Robotics*, 2009, 25(3): 628–633.
[14] M A Ergin, V Patoglu. ASSISTON-SE: A self-aligning shoulder-elbow exoskeleton. *IEEE International Conference on Robotics and Automation*, StPaul, USA, May 14–18, 2012: 2479–2485.
[15] H Yan, C Yang, Y Zhang, et al. Design and validation of a compatible 3-degrees of freedom shoulder exoskeleton with an adaptive center of rotation. *Journal of Mechanical Design*, 2014, 136(7): 071006.
[16] B Dehez, J Sapin. ShouldeRO, an alignment-free two-DOF rehabilitation robot for the shoulder complex. *IEEE International Conference on Rehabilitation Robotics: proceedings*, Zurich, Switzerland, June 27–July 01, 2011: 5975339.
[17] L Cappello, D K Binh, S C Yen, et al. Design and preliminary characterization of a soft wearable exoskeleton for upper limb. *6th IEEE International Conference on Biomedical Robotics and Biomechatronics*, Singapore, June 26–29, 2016: 623–630.
[18] M Hosseini, R Meattini, A San-Millan, et al. A sEMG-driven soft exosuit based on twisted string actuators for elbow assistive applications. *IEEE Robotics and Automation Letters*, 2020, 5(3): 4094–4101.
[19] M Hamaya, T Matsubara, T Teramae, et al. Design of physical user-robot interactions for model identification of soft actuators on exoskeleton robots. *International Journal of Robotics Research*, 2021, 40(1): 397–410.
[20] T T Hoang, L Sy, M Bussu, et al. A wearable soft fabric sleeve for upper limb augmentation. *Sensors*, 2021, 21(22): 7638.
[21] VA Dung Cai, P Bidaud. Self-adjusting isostatic exoskeleton for the elbow joint: Mechanical design. *20th CISM-IFToMM Symposium on Theory and Practice of Robots and Manipulators*, Moscow, Russia, June 23–26, 2014: 19–26.
[22] W X Zhang, S D Zhang, M Ceccarelli, et al. Design and kinematic analysis of a novel metamorphic mechanism for lower limb rehabilitation. *3rd IEEE/IFToMM/ASME International Conference on Reconfigurable Mechanisms and Robots*, Beijing, China, July 20-22, 2015: 545–558.
[23] Y Yu, W Y Liang. Manipulability inclusive principle for hip joint assistive mechanism design optimization. *International Journal of Advanced Manufacturing Technology*, 2014, 70(5–8): 929–945.
[24] J Klein, S Spencer, J Allington, et al. Optimization of a parallel shoulder mechanism to achieve a high-force, low-mass, robotic-arm exoskeleton. *IEEE Transactions on Robotics*, 2010, 26(4): 710–715.
[25] J Hunt, H Lee, P Artemiadis, et al. A novel shoulder exoskeleton robot using parallel actuation and a passive slip interface. *Journal of Mechanisms & Robotics*, 2017, 9(1): 011002.
[26] X L Yang, H T Wu, Y Li, et al. Dynamics and isotropic control of parallel mechanisms for vibration isolation. *IEEE-Asme Transactions on Mechatronics*, 2020, 25(4): 2027–2034.
[27] B Beigzadeh, M Ilami, S Najafian, et al. Design and development of one degree of freedom upper limb exoskeleton. *3rd RSI/ISM International Conference on Robotics and Mechatronics*, Tehran, Iran, October 7–9, 2015: 223–228.
[28] J T Newkrirk, M M Stanisic. Design of a humanoid shoulder complex emulating human shoulder girdle motion using the minimum number of actuators. *International Journal of Humanoid Robotics*, 2016, 13(4): 1550045.
[29] E Culham, M Peat. Functional anatomy of the shoulder complex. *J Orthop Sports Phys Ther*, 1993, 18(1): 342–350.
[30] Y Qi, T Sun, Y Song, et al. Topology synthesis of three-legged spherical parallel manipulators employing Lie group theory. *ARCHIVE Proceedings of the Institution of Mechanical Engineers Part C Journal of Mechanical Engineering Science 1989-1996*, 2014, 229(10): 1873–1886.
[31] Y Cao, H Zhou, Y L Qin, et al. Type synthesis and type analysis of 3T2R hybrid mechanisms via GF set. *International Journal of Robotics & Automation*, 2017, 32(4): 342–350.
[32] Y Fang, L W Tsai. Enumeration of a class of overconstrained mechanisms using the theory of reciprocal screws. *Mechanism and Machine Theory*, 2004, 39(11): 1175–1187.
[33] H S Lo, S Q Xie. Exoskeleton robots for upper-limb rehabilitation: State of the art and future prospects. *Medical Engineering & Physics*, 2012, 34(3): 261–268.
[34] T Geike, J McPhee. Inverse dynamic analysis of parallel manipulators with full mobility. *Mechanism and Machine Theory*, 2003, 38(6): 549–562.
[35] J P Merlet. Jacobian, manipulability, condition number, and accuracy of parallel robots. *Journal of Mechanical Design*, 2006, 128(1): 199–206.
[36] F Pernkopf, M L Husty. Workspace analysis of Stewart-Gough-type parallel manipulators. *Proceedings of the Institution of Mechanical Engineers Part C-Journal of Mechanical Engineering Science*, 2006, 220(7): 1019–1032.
[37] W Huyer, A Neumaier. Global optimization by multilevel coordinate search. *Journal of Global Optimization*, 1999, 14(4): 331–355.
[38] J S Gottschall, R Kram. Energy cost and muscular activity required for propulsion during walking. *Journal of Applied Physiology*, 2003, 94(5): 1766–1772.
[39] J J Cervantes-Sanchez, J M Rico-Martinez, V H Perez-Munoz. Two natural dexterity indices for parallel manipulators: angularity and axiality. *Journal of Mechanisms and Robotics-Transactions of the ASME*, 2014, 6(4): 041007.
[40] M J Song, S Guo, X Y Wang, et al. Dynamic analysis and performance verification of a novel hip prosthetic mechanism. *Chinese Journal of Mechanical Engineering*, 2020, 33(1): 17.